Journal of Materials Chemistry C

PAPER

View Article Online
View Journal | View Issue

Check for updates

Cite this: J. Mater. Chem. C, 2019, 7, 1388

Pressure-induced emission enhancement in hexaphenylsilole: a computational study†

Tian Zhang, [ab] Wen Shi, [b] Dong Wang, [b] Shuping Zhuo, [a] Qian Peng *[c] and Zhigang Shuai *[b]

Organic mechano-responsive luminescent materials have aroused wide attention in recent years for their tremendous utilities. Pressure-induced emission enhancement (PIEE) refers to a novel phenomenon whereby a solid-state luminogen exhibits enhanced emission intensity upon compression, in contrast to the conventional pressure-caused luminescence quenching. The mechanism behind PIEE remains unclear. It is desirable to unravel the effects of pressurization on the optical emission for molecular materials. Here, we carried out an in-depth theoretical investigation on the excited-state decay processes of crystalline hexaphenylsilole (HPS) at high pressure by combining dispersion-corrected density functional theory (DFT-D) crystalline-structure simulations, hybrid quantum mechanics/molecular mechanics (QM/MM) calculations and our thermal vibration correlation function formalism. It was found that the fluorescence quantum efficiency first increases sharply and then levels off as the pressure rises from ambient to 10.86 GPa. This is because the molecular electron–vibration couplings of low-frequency modes (<200 cm^{-1}) are remarkably reduced owing to the pressure-triggered closer molecular packing, slowing down the non-radiative process. When the pressure rises above 5.06 GPa, the electron–vibration couplings of low-frequency modes gradually reach a plateau, although those of high-frequency modes (1400–1800 cm^{-1}) start to decrease slightly, resulting in the saturation of the non-radiative rate constant. Resonance Raman spectroscopy is suggested to probe the above hypothesis in unravelling the PIEE mechanism of HPS. At the same time, a theoretical protocol is proposed to quantitively predict the PIEE properties, thus aiding the rational design of advanced PIEE materials.

Received 12th October 2018,
Accepted 26th December 2018

DOI: 10.1039/c8tc05162c

rsc.li/materials-c

Published on 03 January 2019. Downloaded by Tsinghua University on 2/19/2019 7:51:15 AM.

1. Introduction

Stimuli-responsive luminescent materials have attracted considerable interest owing to their practical applications in optical devices and sensors.[1–6] High pressure technology has been widely used to study the photophysical properties of organic luminescent compounds.[7,8] Generally, it was found that pressurization weakens the emission of organic luminogens in the condensed phase as the intermolecular interactions increase.[9,10] Thus, it is intriguing for organic luminophores exhibiting pressure-induced emission enhancement (PIEE) phenomena. For example, applying a hydrostatic pressure in the range of 1–104 atm to hexaphenylsilole (HPS) film boosts its photoluminescence (PL) intensity by at most 10%.[11] From ambient pressure up to 7 GPa, a series of dicyanovinyl-substituted aromatic compounds dispersed in polymer media show a sharp increase in fluorescence intensities.[12] Exerting hydrostatic pressure in the range of 1.5–5.3 GPa on tetraphenylethene (TPE) crystal leads to a drastic emission enhancement.[13] On compressing triphenylacrylonitrile (β-CN-TPA) crystal with the hydrostatic pressure increasing from 1 atm to 1.1 GPa, its emission intensity is significantly enhanced.[14] Upon compression up to 1.0 GPa, carbazole crystal presents a conspicuous fluorescence enhancement.[15]

PIEE phenomena are quite surprising. Suppression of the intramolecular motion has been proposed to account for the PIEE phenomena.[11,13–15] It was also speculated that a pressure-induced change in molecular conformation is responsible for the enhanced luminescence.[12] However, the detailed structure–property relationship behind PIEE is elusive, largely due to the limited structural and photophysical characterization techniques accessible for high-pressure experiments. To utilize the enhanced efficiency of PIEE and develop more efficient solid-state emitters, an in-depth and comprehensive mechanistic study is urgently desired.

The excited-state dynamics of organic molecular aggregates play fundamental roles in understanding the photophysics of

[a] School of Chemistry and Chemical Engineering, Shandong University of Technology, Zibo 255049, P. R. China
[b] MOE Key Laboratory of Organic OptoElectronics and Molecular Engineering, Department of Chemistry, Tsinghua University, Beijing, 100084, P. R. China. E-mail: zgshuai@tsinghua.edu.cn
[c] CAS Key Laboratory of Organic Solids, Institute of Chemistry, Chinese Academy of Sciences, Beijing 100190, P. R. China. E-mail: qpeng@iccas.ac.cn

† Electronic supplementary information (ESI) available. See DOI: 10.1039/c8tc05162c

This journal is © The Royal Society of Chemistry 2019

Published on 03 January 2019. Downloaded by Tsinghua University on 2/19/2019 7:51:15 AM.

the organic light-emitting solids. The vibrationally resolved optical spectra and excited-state decay rate constants are effective characterizations for exploring the luminescent mechanism. A theoretical mechanistic study of PIEE can reveal the structure and excited-state dynamics information at different pressure values. Experimentally, the hydrostatic pressure imposed on the sample is homogeneous. Therefore, the hydrostatic compression process can be simplified by volume contraction of the crystal lattice computationally. From this point of view, dispersion-corrected density functional theory (DFT-D) based on the plane-wave basis offers an effective way to reproduce the crystal structure at a given external pressure.[16,17] Based on that, the investigation of the excited-state dynamics for the molecular aggregates in organic crystals can be realized by our group through thermal vibration correlation function formalism coupled with hybrid quantum mechanics/molecular mechanics (QM/MM) simulations.[18–20]

In this work, we adopt a theoretical protocol to investigate the excited-state decay processes of organic crystals at high pressure, which combines DFT-D calculations, a QM/MM approach and the thermal vibration correlation function formalism. DFT-D calculations are performed to determine the crystalline structures at hydrostatic pressure. The QM/MM approach is adopted to obtain the molecular electronic structure and electron–vibration couplings in the aggregates. Thermal vibration correlation function formalism is applied to calculate the related optical spectra and excited-state decay rate constants. By using this protocol, we systematically unravel the pressurization effect on the photophysical properties of an emblematic PIEE luminogen, HPS (Chart 1). We aim to elucidate the exact roles of intra- and inter-molecular interactions in the PIEE materials composed of such propeller-shaped molecules as HPS. The resonance Raman spectra at ambient and high pressures are also predicted to probe the pressurization effect on the non-radiative vibrational relaxation.

2. Computational methods

2.1 DFT-D calculations

In order to obtain the single-crystal structures of HPS at different hydrostatic pressures, we performed DFT-D calculations as implemented in the Vienna Ab initio Simulation Package (VASP 5.3.2).[21,22] The projector augmented wave (PAW)[23] method with the Perdew–Burke–Ernzerhof exchange–correlation functional including dispersion (PBE-D2)[24] was chosen for both geometry optimizations and single-point energy calculations. We started the crystalline structure simulations with the configuration from the X-ray diffraction at ambient pressure. Both atomic positions and the lattice constants were relaxed during geometry optimizations. The cut-off energy for the plane-wave basis was set to be 400 eV. A k-mesh of $2 \times 2 \times 1$ was used for the self-consistent field calculations. The energy tolerance for electronic relaxation convergence was set to be 10^{-5} eV with a force tolerance of 0.01 eV Å^{-1}. The spin–orbit coupling and spin-polarization were not considered. The cut-off radius for pair interactions was set to be 50 Å. Based on the optimized structure, we set the cut-off energy to be 600 eV and chose a denser k-mesh of $4 \times 4 \times 2$ for the single-point energy calculation to obtain the stress. Then we minimized the initial crystal by scaling the lengths of a, b, and c along three lattice vectors in random proportions of 1.0, 0.995, 0.99, 0.98, 0.95, 0.92, 0.90, and 0.89. We also performed the same optimization and single-point energy calculations on these contracted lattices to obtain the relaxed crystal structure under a given high stress. Finally, the pressure of optimized crystal structure without contraction is set to be ambient (0 GPa). To verify the reliability of the above computation scheme to achieve single crystals at hydrostatic compression conditions for organic crystals, we applied this simulation framework to naphthalene, whose crystallographic lattice constants at high pressure are accessible. Good agreement was found between theoretical values and experimental results with all errors within 5.5% (Table S1, ESI†).

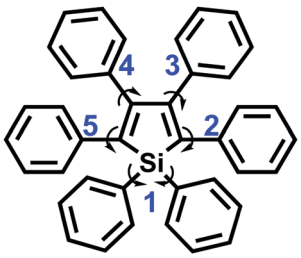

Chart 1 Molecular structure of HPS with torsional angles marked by numbers and arrows.

2.2 QM/MM simulations

On the basis of the crystal structures obtained from DFT-D calculations, we set up the QM/MM models for each HPS aggregate at both ambient and high pressures. The QM/MM model was built by cutting a cluster from the crystal of size $5 \times 3 \times 3$. The central molecule (71 atoms) was treated as the QM region and others were all MM molecules (5254 atoms) (Chart 2). During the QM/MM simulations, geometry optimizations were performed on the QM molecule with the MM molecules frozen. The QM/MM energy and gradient calculations were carried out in the ChemShell[25] package, interfacing the Turbomole[26] program for QM and the DL_POLY[27] program for MM. The electrostatic and van der Waals interactions between the QM and MM regions were considered in the embedded scheme[28] and Lennard-Jones formalism, respectively. We adopted (TD)-B3LYP[29,30]/6-31G(d) for QM and the general Amber force field (GAFF)[31] for MM, which has been proved to be a reliable level to treat the excited-state decay processes of crystalline and amorphous HPS aggregates.[32–34] The vibrational frequencies were obtained with the numerical two-point differentiation approach. Translational and rotational spaces were projected out for all Hessian calculations through Gram–Schmidt orthogonalization.[35] The above QM/MM approach has been shown to be very successful in dealing with the electronic structures and transition properties of various organic aggregates besides the siloles, including pyrazine derivatives, stilbene derivatives and the sexithiophene (6T) nanoparticle.[18–20,36,37] To estimate the intermolecular excitonic effects, we calculated the excitonic couplings (J)[38] of different dimers in HPS aggregates using the tools in the

Published on 03 January 2019. Downloaded by Tsinghua University on 2/19/2019 7:51:15 AM.

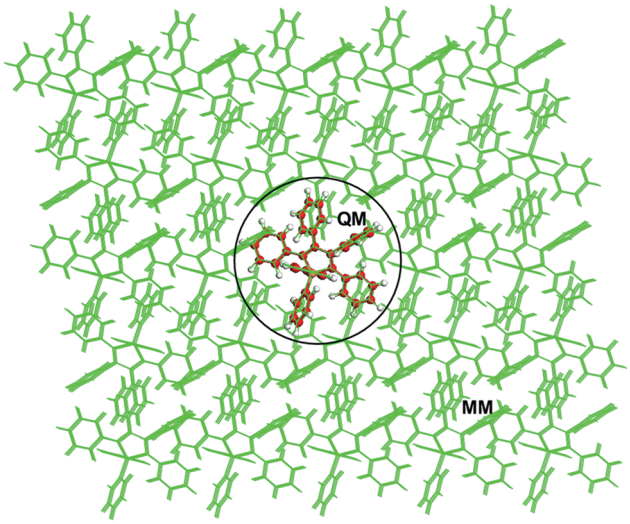

Chart 2 Setup of the QM/MM model.

MOMAP[39] program with the excitation information generated from TD-DFT calculations in the NWChem[40] package at the CAM-B3LYP[41]/6-31G(d) level. Moreover, we also performed single-point TD-DFT calculations for the dimers with maximum J at 0 GPa and 5.06 GPa, respectively. It was found that there are only local excitations without any intermolecular charge transfer (CT) character (Fig. S1, ESI†), which is consistent with the experimentally observed emission spectra without very large red-shifts with increasing pressure.[11]

2.3 Excited-state decay theory with correlation function formalism

The absorption $\sigma_{ab}(\omega,T)$ and emission $\sigma_{em}(\omega,T)$ spectra can be written as:

$$\sigma_{ab}(\omega,T)=\frac{4\pi^2\omega}{3\hbar c}\sum_{u,\nu}P_{i\nu}(T)|\langle\Theta_{fu}|\vec{\mu}_{fi}|\Theta_{i\nu}\rangle|^2\delta(\omega-\omega_{fu,i\nu}) \quad (1)$$

$$\sigma_{em}(\omega,T)=\frac{4\omega^3}{3\hbar c^3}\sum_{u,\nu}P_{i\nu}(T)|\langle\Theta_{fu}|\vec{\mu}_{fi}|\Theta_{i\nu}\rangle|^2\delta(\omega_{i\nu,fu}-\omega) \quad (2)$$

where $P_{i\nu}(T)$is the initial-state Boltzmann distribution function and Θ is the nuclear vibrational wave function. $\vec{u}_{fi}$ is the electric transition dipole moment between the two electronic states $|\Phi_i\rangle$ and $|\Phi_f\rangle$, which becomes $\vec{u}_0$ independent of the nuclear coordinate under the Franck–Condon approximation. Fourier transforming the delta functions in eqn (1) and (2), the analytical integral formalisms are obtained:

$$\sigma_{ab}^{FC}(\omega,T)=\frac{2\pi\omega}{3\hbar c}|\vec{\mu}_0|^2\int_{-\infty}^{\infty}e^{i(\omega-\omega_{fi})t}Z_i^{-1}\rho_{ab,0}^{FC}(t,T)dt \quad (3)$$

$$\sigma_{em}^{FC}(\omega,T)=\frac{2\omega^3}{3\pi\hbar c^3}|\vec{\mu}_0|^2\int_{-\infty}^{\infty}e^{-i(\omega-\omega_{if})t}Z_i^{-1}\rho_{em,0}^{FC}(t,T)dt \quad (4)$$

where Z_i is the partition function. $\rho_{ab,0}^{FC}(t,T)$ and $\rho_{em,0}^{FC}(t,T)$ are the thermal vibration correlation functions.[19,42]

The radiative rate constant can be formulated as an integral over the whole emission spectrum:

$$k_r(T)=\int\sigma_{em}(\omega,T)d\omega \quad (5)$$

Based on perturbation theory and Fermi's golden rule, the analytical formalism of the non-radiative internal conversion rate constant (k_{ic}) can be expressed as:

$$k_{ic}=\sum_{kl}\frac{1}{\hbar^2}R_{kl}\int_{-\infty}^{\infty}\left[e^{i\omega_{if}t}Z_i^{-1}\rho_{ic,kl}(t,T)\right]dt \quad (6)$$

where $\rho_{ic,kl}(t,T)$ is the correlation function part.[19,42,43] First-order perturbation theory following Lin[44] was applied to compute the non-adiabatic electronic couplings related to R_{kl}. Note that the rate formalism is not suitable for treating the excited-state decay *via* a conical intersection.[19] The conical intersection mediated decay time is usually in the order of femtoseconds or picoseconds, much faster than the fluorescence radiative decay time in the order of nanoseconds.

Based on the structure and Hessian information of the ground (g) and excited (e) states obtained from the QM/MM simulations, we calculated the absorption and emission spectra, and the radiative and non-radiative rate constants through the MOMAP program by solving the above eqn (3)–(6). The differences between the potential energy surfaces (PES) in the g and e states are considered by the relationship of the normal-mode coordinates $Q_e = MQ_g + D_e$, where $M = L_e^T L_g$ is the Duschinsky rotation matrix (DRM) and $D_e = L_e^T\Delta q$ is the displacement vector connecting the minima of the parabolas of g and e. $L_{g(e)}$ is the eigenvector of the mass-weighed Hessian matrix of the g(e) state, and Δq is the shift in the mass-weighed Cartesian coordinates of g and e.

2.4 Resonance Raman spectroscopy with Green's function formalism

The resonance Raman scattering cross section $\sigma(\omega_I,\omega_S)$ is given as follows:

$$\sigma(\omega_I,\omega_S)\propto\omega_I\omega_S{}^3S(\omega_I,\omega_S) \quad (7)$$

where ω_I is the frequency of the incident light and ω_S is the frequency of the scattered light. The line shape $S(\omega_I,\omega_S)$ can be written as:

$$S(\omega_I,\omega_S)=2\pi\sum_{m,n}P(n)|\hat{e}_S\cdot\alpha_{mn}\cdot\hat{e}_I|^2\delta(\omega_S-\omega_I-\varepsilon_n+\varepsilon_m) \quad (8)$$

$\hat{e}_I$ and $\hat{e}_S$ indicate the polarization directions of the incident and scattered light, respectively. ε_n and ε_m are the vibrational energies in the electronic ground state, and again $P(n)$ is the probability of the initial state n. α_{mn} is the Kramers–Heisenberg–Dirac (KHD) polarizability tensor.

For strong-dipole allowed transition, only the Frank–Condon (FC) term α_{mn}^{FC} is considered by approximation. By transforming α_{mn}^{FC} into the time domain using Green's function, the following analytical expression is obtained:

$$\alpha_{mn}^{FC}=i|\vec{\mu}_0|^2\int_0^{\infty}G_{mn}(t)\exp\left[i(\omega_I-\omega_{eg}+\varepsilon_n)t-\gamma t\right]dt \quad (9)$$

This journal is © The Royal Society of Chemistry 2019

Published on 03 January 2019. Downloaded by Tsinghua University on 2/19/2019 7:51:15 AM.

where ω_{eg} is the electronic adiabatic energy difference. γ is the damping constant of the excited state. $G_{mn}(t)$ has an analytical solution for the jth single-mode excitation from n to m.[45]

The resonance Raman spectra at different pressures were calculated using the RRS[46] program by solving the above eqn (7)–(9). The required molecular structure and Hessian matrix are the same as those substituted into the formula for calculations of the spectra and rate constants. The mode distortion and Duschinsky rotation effect (DRE) are also included. 100 cm^{-1} and 10 cm^{-1} are adopted for γ and Lorentz broadening of the delta function, respectively. The incident wavelength is chosen to be equal to the electronic adiabatic energy gap at a given pressure value.

3. Results and discussion

3.1 Intermolecular and intramolecular structures

The lattice constants of the unit cell of the HPS crystal at different pressures are listed in Table S2 (ESI†). The optimized structure is in good agreement with the single-crystal diffraction data at ambient pressure. The variation of the unit-cell volume with respect to pressure is shown in Fig. 1a. The volume is continuously reduced with increasing pressure, indicating that the stable structure remains up to 10.86 GPa and experiences no phase transition. The *a*, *b*, and *c* lengths decrease monotonically but with different rates (inset, Fig. 1a), which demonstrates the anisotropic compression of HPS under pressure. The *b*-axis is more compressible than the *a*- and *c*-axes, leading to the molecules nearly parallel to the *ac* plane packing closer (Fig. 1b). Accordingly, the intermolecular distances of the HPS aggregates in our QM/MM models are reduced with the compression stress (Fig. S2, ESI†), implying pressure-promoted intermolecular interactions.

To visualize the detailed intermolecular interaction in the HPS aggregates at both ambient and high pressures, the reduced density gradient (RDG) method is used.[47] The intermolecular C–H···π hydrogen bond, π–π stacking interaction and steric hindrance between the QM molecule and surrounding MM molecules were identified and are illustrated in Fig. 2. Upon compression, there appear more and stronger C–H···π hydrogen bond (blue region) and steric hindrance (red region) accompanied by the enhanced π–π interaction (green region). The formation and further strengthening of the aromatic C–H···π hydrogen bonds and steric effects from the surrounding MM molecules would constrain the phenyl movements of the QM molecule.

To explore the effect of the enhanced intermolecular interactions on the intramolecular structure, we firstly analyzed the electronic properties of the molecular excited state. We found that the transitions are mostly HOMO → LUMO transition at both ambient and high pressures (Table S3, ESI†). The electronic density is distributed mainly on rings at the 2,5-positions adjacent to the central silacycle, with minors on the ring at the 3-position, tiny on ring at the 4-position and almost none on rings at the 1,1-positions (Fig. 3). Therefore, the dihedral angles at the 2,3,4,5-positions (Fig. S3, ESI†) of HPS are presented in Table 1, with the geometric parameters at the optimized S_0/S_1 states and the modifications between the two states upon excitation. As shown in our previous work,[32,34] the behavior of the phenyl rings at the 2,5-positions of HPS mainly dominates the solid-state optical properties. It can be seen that the dihedral modification at 2,5-positions exhibits a gradual reduction when pressure is increased from ambient to 5.06 GPa, then it exhibits a slight increase from 5.06 to 10.86 GPa. The structural change at the 3-position keeps decreasing with pressure but that at the 4-position is not regular. This suggests that the torsional motions of the phenyls at the significant 2,5-positions are firstly hindered then slightly active with the elevated pressure, while the phenyl at the 3-position is always restricted.

3.2 Optical spectra and fluorescence quantum efficiency

The optical properties of the crystalline aggregates are governed by the competition between the intermolecular excitonic coupling J and the intramolecular relaxation energy $\lambda_{g(e)}$. The J characterizes

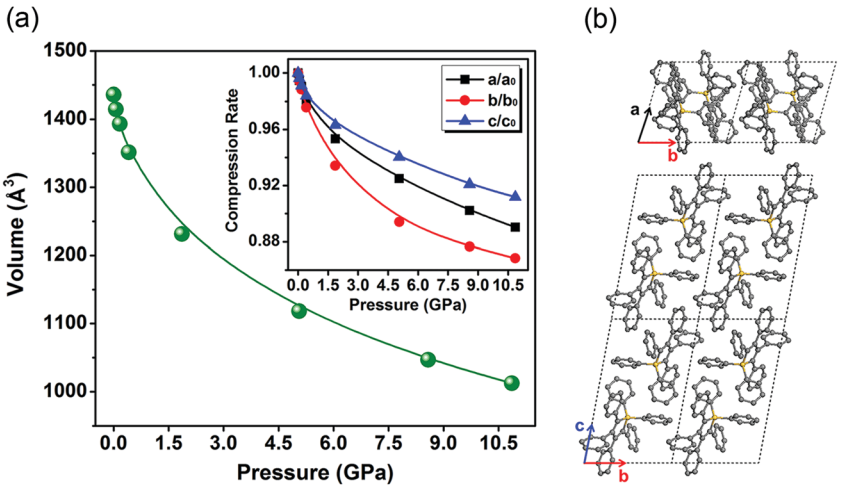

Fig. 1 (a) Compression of the unit-cell volume of HPS with increasing pressure. The inset shows the compression rate of the lattice lengths at different pressures. (b) Arrangement of HPS in the *ab* and *bc* planes. The black dashed lines represent the crystal lattices and the hydrogen atoms have been removed for the sake of clarity.

Published on 03 January 2019. Downloaded by Tsinghua University on 2/19/2019 7:51:15 AM.

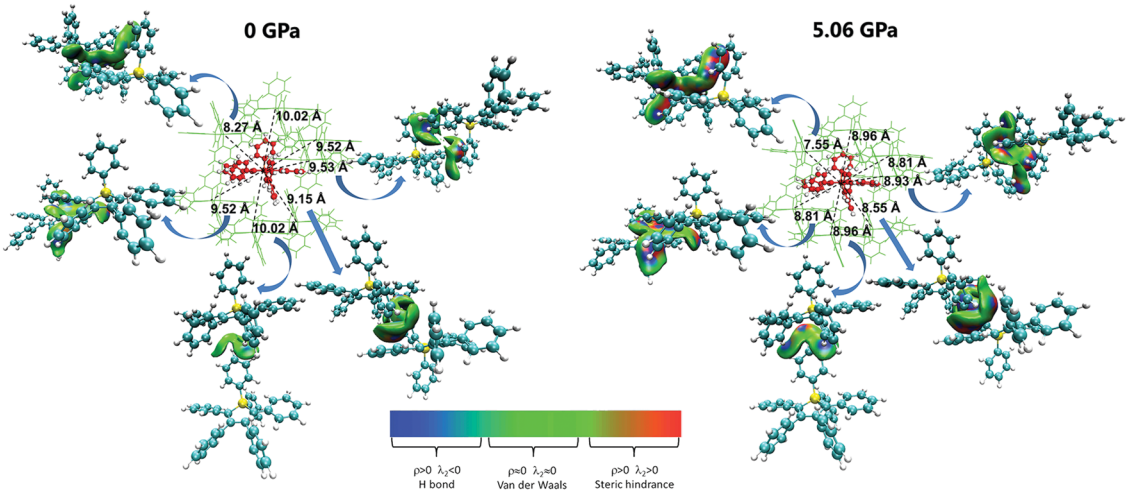

Fig. 2 Molecular packing structures within ~10 Å of the QM centroid and relevant intermolecular interactions in the HPS aggregates at 0 GPa and 5.06 GPa.

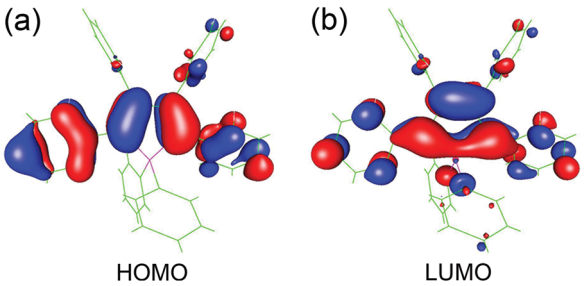

Fig. 3 Electron density contours of HOMO (a) and LUMO (b) for HPS in aggregates.

the degree of intermolecular excited-state interaction, which is determined by the intermolecular distance and transition dipole moment. $\lambda_{g(e)}$ in the ground-state (excited-state) PES (Fig. S4, ESI†) measures the extent of intramolecular electron–vibration coupling, which is reflected by the geometrical modification upon absorbing or emitting a phonon between two electronic states. The calculated J and $\lambda_{g(e)}$ are presented in Table S4 (ESI†) and plotted in Fig. 4. Note the maximum J among different dimers is chosen to be the representative; other values at ambient pressure can be found in Table S5 (ESI†). It can be seen that the values of J are at least one order of magnitude smaller than $\lambda_{g(e)}$ and the ratios of $J/\lambda_{g(e)}$ are always less than the critical value of 0.17 at different pressures. Thus, their optical properties are independent of J and determined by $\lambda_{g(e)}$,[48] and J can be neglected in the subsequent calculations of the vibrationally resolved spectra and excited-state decay rate constants.

The calculated vibrationally resolved absorption and emission spectra at different pressures are shown in Fig. 5. Remarkable red-shifts can be observed in the absorption bands of compressed HPS with the pressure elevated from ambient to 10.86 GPa but almost no shifts are found in emission except for the minor red-shift over 5.06 GPa. The former red-shifted absorption is ascribed to the pressurization effect on the frontier molecular orbitals, which is supported by the smaller HOMO–LUMO energy gaps at the S_0 equilibrium geometries upon compression (Table S6, ESI†). The latter almost unaffected peak positions in emission at high pressure are consistent with the previous experimental findings by Fan *et al.*[11] whereby the PL peak of the HPS film is insensitive to pressure even as high as 550 atm. It should be mentioned that the magnitude of the pressure we applied to the HPS crystal in the calculation is several GPa but that the pressure exerted onto the HPS film experimentally is hundreds of atm. The difference could be attributed to the tighter molecular packing and stronger intermolecular interactions

Table 1 Selected dihedral angles (in deg.) of HPS in aggregates at different pressures. S_0/S_1 and Δ represent the geometric parameters extracted from the optimized S_0/S_1 states and the modifications between the two states, respectively

	S_0	S_1	Δ	S_0	S_1	Δ	S_0	S_1	Δ	S_0	S_1	Δ
	0 GPa			0.06 GPa			0.17 GPa			0.41 GPa		
2	42.53	38.17	4.36	41.21	37.22	3.99	41.02	37.22	3.80	38.47	35.28	3.19
5	−1.01	1.20	2.21	−0.95	0.93	1.88	−1.16	0.39	1.55	−1.65	−0.62	1.03
3	63.51	56.56	6.95	63.22	56.82	6.40	63.06	56.84	6.22	62.30	57.08	5.22
4	83.29	82.90	0.39	83.39	83.62	0.23	83.84	85.16	1.32	84.65	87.18	2.53
	1.86 GPa			5.06 GPa			8.58 GPa			10.86 GPa		
2	34.69	32.55	2.14	32.97	31.20	1.77	30.55	28.54	2.01	28.31	26.26	2.05
5	−2.60	−2.17	0.43	−3.79	−4.15	0.36	−5.45	−6.70	1.25	−6.85	−8.67	1.82
3	61.12	57.67	3.45	61.38	59.10	2.28	61.95	60.31	1.64	61.46	60.16	1.30
4	85.43	88.66	3.23	84.85	87.68	2.83	83.55	86.42	2.87	83.56	86.61	3.05

 This journal is © The Royal Society of Chemistry 2019

Published on 03 January 2019. Downloaded by Tsinghua University on 2/19/2019 7:51:15 AM.

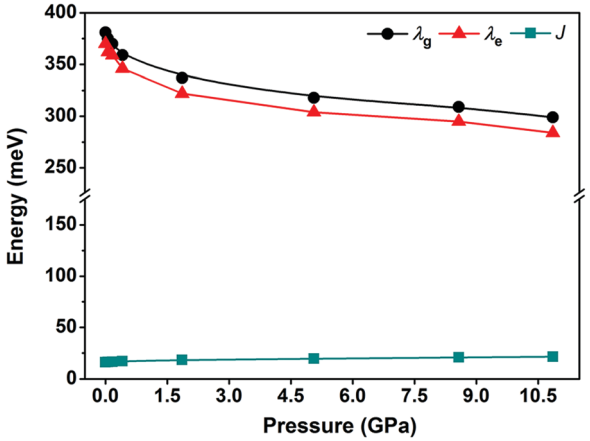

Fig. 4 Relaxation energies $\lambda_{g(e)}$ and excitonic couplings J of HPS in aggregates at different pressures.

in the crystal than in the film so that merely a much higher pressure applied to the crystal is capable of inducing a similar deformation extent to that in the film. The vibronic features are also more significant in both absorption and emission band shapes during the compression process, hinting that the molecular structures are more rigid with the strengthened intermolecular interactions. Moreover, the mirror-image symmetry between the absorption and emission spectra at each pressure is broken, owing to the distortion and Duschinsky rotation effects between the S_0 and S_1 PESs.[49]

The fluorescence quantum efficiency (Φ_F) is determined by the competition between the radiative and non-radiative rate constants (k_r and k_{nr}) with the definition of $\Phi_F = k_r/(k_r + k_{nr})$. k_{nr} includes k_{ic} and the intersystem crossing rate constant (k_{isc}). We ignore k_{isc} owing to the considerably large energy gap (>1 eV) and negligibly small (~ 0.1 cm^{-1}) spin–orbit coupling of HPS in aggregates between the S_1 and T_1 states, as shown previously.[32,33] The calculated k_r, k_{ic} and Φ_F are listed in Table 2. k_r varies slightly with the increase of pressure, while k_{ic} decreases rapidly first in the pressure range of 0 to 5.06 GPa then levels off beyond 5.06 GPa. Correspondingly, Φ_F rises swiftly with pressure up to 5.06 GPa but

Table 2 The calculated k_r, k_{ic} and Φ_F of HPS in aggregates at different pressures

Pressure (GPa)	k_r (10^7 s^{-1})	k_{ic} (10^7 s^{-1})	Φ_F (%)
0	6.47	1.58	80.4
0.06	6.61	1.02	86.6
0.17	6.65	0.70	90.5
0.41	6.79	0.48	93.5
1.86	6.78	0.28	96.1
5.06	6.72	0.21	96.9
8.58	6.77	0.21	97.0
10.86	6.55	0.20	97.0

tends to be constant at higher pressures (Fig. 6). The calculated results roughly agree with the experimental fact that the PL intensity of the compressed HPS film speeds up with increasing pressure up to 104 atm but then begins to decrease slowly with further pressurization. Note that the PL intensities in the descendent region at higher pressures (104–550 atm) are still larger than that at ambient pressure. The calculated flat Φ_F in the higher pressure range (>5.06 GPa) could be ascribed to the formation of favorable excimeric species as promoted by the effective intermolecular π–π stacking interactions,[13,15] which is not considered and is beyond reach at the moment in our computational studies of excited-state dynamics for aggregates. Nevertheless, the PIEE fact has been well reproduced.

3.3 Pressurization effects on electron–vibration couplings and excited-state geometry relaxations

To gain deeper insight into the exotic PIEE phenomena, we analyzed the main factors affecting k_r and k_{ic}. From the Einstein spontaneous emission relationship, k_r is proportional to the adiabatic excitation energy (ΔE) and the electric transition dipole moment (μ). Thus, k_r is insensitive to pressure as both ΔE and μ undergo slight modifications (Table S3, ESI†). In contrast to the radiative decay, the non-radiative decay dissipates the electronic excited-state energy into vibrational reorganization. Thus, the non-radiative process is mainly determined by the non-adiabatic electronic coupling, the electron–vibration coupling

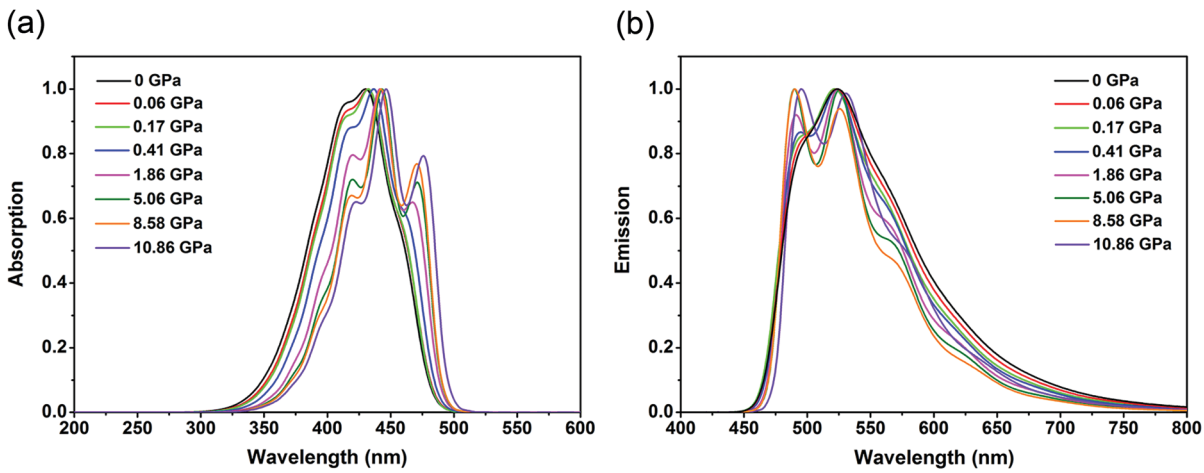

Fig. 5 Calculated vibrationally resolved normalized absorption (a) and emission (b) spectra for HPS in aggregates at different pressures.

Published on 03 January 2019. Downloaded by Tsinghua University on 2/19/2019 7:51:15 AM.

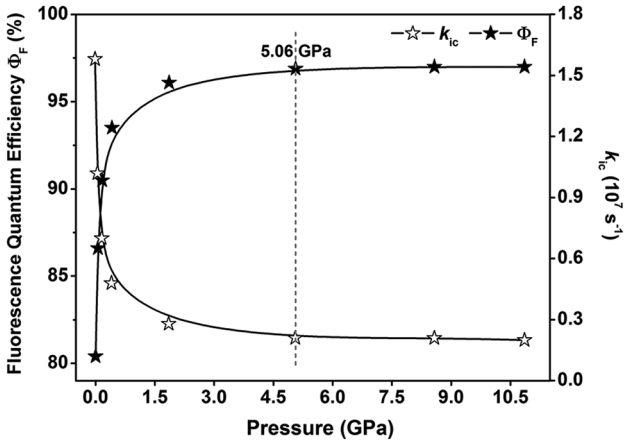

Fig. 6 Calculated k_{ic} and Φ_F of HPS in aggregates at different pressures.

and the DRE. We then plot the diagonal part R_{kk} of the electronic coupling matrix elements R_{kl} at different pressures in Fig. S5 (ESI†). Although there is a slight difference in the distributions, the summation of R_{kk} is very close and hardly varies upon compression. The electron–vibration coupling is also called the relaxation energy λ, which demonstrates the vibrations' ability to accept the excited-state electronic energy. Based on the harmonic oscillator approximation, the λ_j of the jth normal mode is defined as its energy $\hbar\omega_j$ multiplied by the corresponding Huang–Rhys factor S_j, $\lambda_j = \hbar S_j \omega_j = \frac{1}{2} D_j^2 \omega_j^2$. D_j is the displacement along the jth normal mode between two electronic states. When considering the difference between the PESs in the ground and excited states, there are two sets of relaxation energy, $\lambda_{j,g}$ and $\lambda_{j,e}$. The total relaxation energy with the summation of all normal modes is λ_g and λ_e. As seen from Fig. 4, $\lambda_{g(e)}$ decreases with pressure,

Table 3 Relaxation energies of low-frequency modes (λ_{LF}) and high-frequency modes (λ_{HF}), as well as their contributions to the total λ_g for HPS in aggregates at different pressures

Pressure (GPa)	λ_{LF} (meV)	λ_{HF} (meV)	λ_g (meV)	λ_{LF}/λ_g	λ_{HF}/λ_g
0	71	204	381	0.19	0.54
0.06	66	203	375	0.18	0.54
0.17	61	203	370	0.16	0.55
0.41	53	200	359	0.15	0.56
1.86	26	191	337	0.08	0.57
5.06	17	180	318	0.05	0.57
8.58	16	169	309	0.05	0.55
10.86	16	160	299	0.05	0.54

which implies that molecular packing restricts the intramolecular vibrational reorganization and then reduces k_{ic}. λ_j *versus* ω_j at different pressures is shown in Fig. 7a (Fig. S6a, ESI† for the excited-state situation). The normal mode analyses were done with the EVC module embedded in the MOMAP program. We find that the contribution of low-frequency (LF, <200 cm^{-1}) modes to the total λ_g gradually decreased from 19% to 5% in the lower pressure range of 0–5.06 GPa but starts to be fixed at 5% in the higher pressure range over 5.06 GPa (Table 3), while the contribution of high-frequency (HF, 1400–1800 cm^{-1}) modes varies slightly with 54–57% in the whole pressure range. Similar contributions are found for λ_e (Table S7, ESI†). S_j *versus* ω_j are also shown in Fig. 7b (Fig. S6b, ESI† for the excited-state situation), which characterizes the vibrational quanta absorbed or emitted in the excited-state relaxation process. It is more obvious and straightforward that the S_j of low-frequency modes are remarkably reduced with increasing pressure. When the pressure rises over 5.06 GPa, the S_j of low-frequency modes gradually reaches a plateau although those of high-frequency modes start to decrease slightly. Therefore, the decrease in $\lambda_{g(e)}$ upon compression mainly stems from the reduced S_j of the low-frequency modes. The DRE measures the coupling

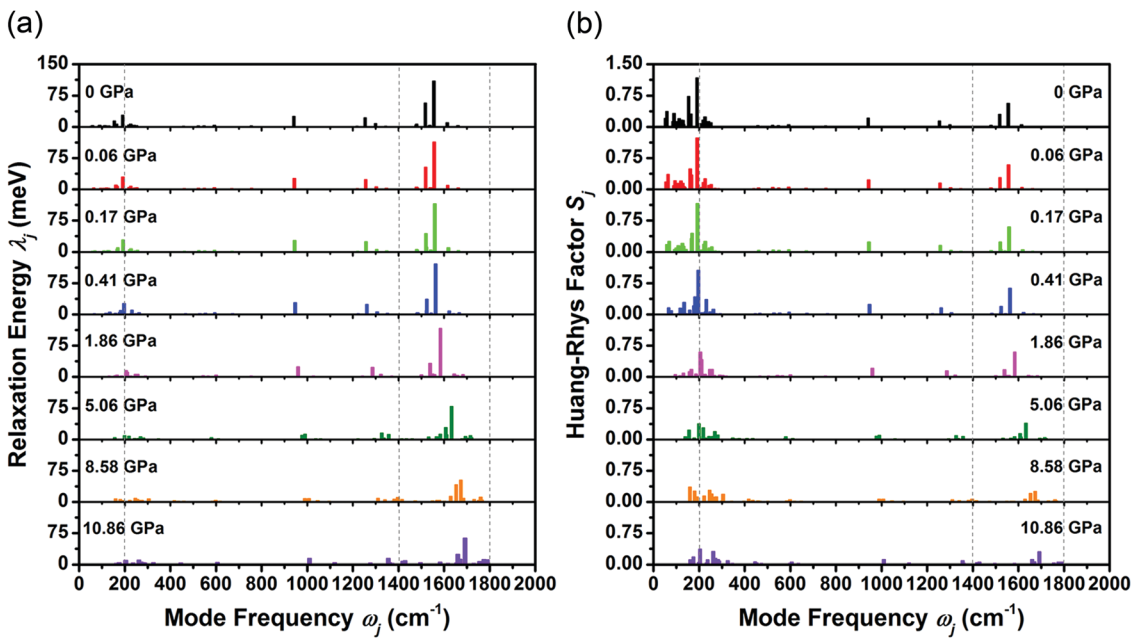

Fig. 7 Relaxation energy λ_j (a) and Huang–Rhys factor S_j (b) of each normal mode *versus* mode frequency ω_j of HPS in aggregates at different pressures.

 This journal is © The Royal Society of Chemistry 2019

Published on 03 January 2019. Downloaded by Tsinghua University on 2/19/2019 7:51:15 AM.

among multiple vibrational modes and the serious DRE can largely accelerate the non-radiative decay rate. The DRE can be directly characterized from the calculated DRM. Since the DRE occurs most remarkably for low-frequency modes according to our previous investigations,[19,20,43] we presented the contour maps of the DRM for the lowest 20 normal modes (Fig. S7, ESI†). The larger the values of the off-diagonal elements are, the more severe the DRE is. As the pressure increases from 0 to 5.06 GPa, many off-diagonal elements of the DRM become null, corresponding to the decoupling among modes, thus decreasing k_{ic}. However, the off-diagonal elements experience little changes with further compression (>5.06 GPa), indicating no further lessening effects on k_{ic} through the DRE. All the above indicates that the continuously enhanced luminescence from 0 to 5.06 GPa arises from the restraint of intramolecular rotations (rings out-of-plane twisting, Fig. S8 and Table S8, ESI†) in the low-frequency regime. Excessive compression beyond 5.06 GPa begins to suppress molecular vibrations (CC stretching, CCC and CH in-plane bending, Fig. S8 and Table S8, ESI†) in the high-frequency region but has no further boosting effect on the luminescence efficiency. The restricted low-frequency vibrational motions have been shown to dominate the aggregation-induced emission (AIE) process of HPS in our previous work;[32,34] therefore, the PIEE fully supports the cause of its AIE effect.

As shown in our previous work,[50] resonance Raman spectroscopy has been theoretically proposed to verify the restricted non-radiative relaxation hypothesis in explaining the AIE mechanism. The frequency resonance not only enhances the Raman signal, but also reveals the mode-specific relaxation energy during the excited-state relaxation process in different environments. The resonance Raman intensity is proportional to the relaxation energy of each mode λ_j multiplied by the frequency ω_j.[50–52] Thus, the calculated resonance Raman spectra are conducted to make the relaxation energy observed intuitively at different pressures and further clearly unravel the PIEE mechanism. At the same time, this would provide some comparative results for direct experimental confirmation.

The calculated resonance Raman spectra at different pressures are depicted in Fig. 8. It can be seen that the spectra resemble the "signatures" of the relaxation energy columns in Fig. 7a. All Raman peaks at high pressure show blue-shifts compared to the ambient condition. The blue-shifts in the low-frequency regime (<200 cm^{-1}) major at 0–5.06 GPa, indicating that the intramolecular rotations are dampened by the closer molecular packing induced by pressure, whereas the remarkable blue-shifts and weakening intensities of the Raman peaks in the high-frequency region (1400–1800 cm^{-1}) major at and over 5.06 GPa, illustrating that vibration relaxations are suppressed upon compression. Therefore, the resonance Raman spectra we predicted here are shown to be valuable and hold potential for the characterization of the pressurization effect on the non-radiative vibrational relaxation. Actually, the Raman peaks shifting to the region of >200 cm^{-1} with increasing pressure are more sensitive and easier to measure experimentally.[53]

To figure out the relationship between the excited-state energy dissipation pathways and molecular geometry modifications, we

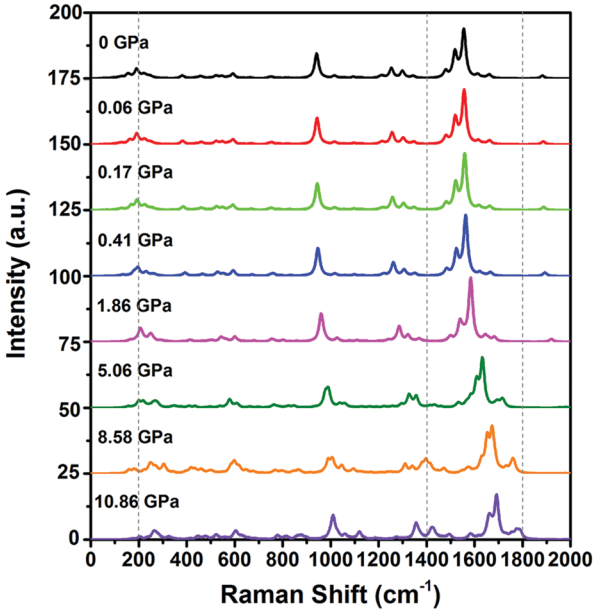

Fig. 8 The calculated resonance Raman spectra of HPS in aggregates at different pressures.

projected the total relaxation energy onto the molecular bond length (λ_{bond}), bond angle (λ_{angle}) and dihedral angle ($\lambda_{dihedral}$).[54] The contributions from these internal coordinates of HPS in aggregates at different pressures are depicted in Fig. 9 (Fig. S9, ESI† for the excited-state situation) and listed in Table S9 (ESI†). It can be seen that λ_{bond} stays almost unchanged first and then decreases substantially with pressure, in accordance with λ_{HF} (Table 3). $\lambda_{dihedral}$ declines gradually in the lower pressure range of 0–5.06 GPa but experiences a slight increase at higher pressures (>5.06 GPa). This indicates that pressurization first acts on $\lambda_{dihedral}$ (out-of-plane torsional motions) and then on λ_{bond} (bond stretching). With closer intermolecular packing (Fig. 2), the steric hindrance is enhanced and there is less and less space for the phenyls to rotate, thus $\lambda_{dihedral}$ decreases. Excessive pressurization begins to squeeze the bonds, then λ_{bond} decreases and $\lambda_{dihedral}$ slightly increases since the squeezed bonds vacate the additional tiny space. λ_{angle} fluctuates in a very small range of values, implying that pressurization has little effect on the in-plane bending vibrations. Notably, $\lambda_{dihedral}$ also reflects the torsional modifications between the S_0 and S_1 states. As presented in Table 1, the gradual decrease of $\lambda_{dihedral}$ at lower pressures mainly arises from the continuously suppressed torsional motions of the phenyls at the 2,3,5-positions, while the small increase of $\lambda_{dihedral}$ at higher pressures is due to the competitive consequence of the active phenyls at the 2,5-positions and the still hindered phenyl at the 3-position. This also clearly reveals from the geometry relaxation insight that the PIEE of HPS is attributed to the pressure-triggered restrictions imposed on molecular rotations associated with the variations of the dihedral angles, rather than the suppressions acting on molecular vibrations related to the modifications of the bond lengths.

In addition to the above-stated non-radiative decay channels induced by intramolecular thermal vibrations, other deactivation

Published on 03 January 2019. Downloaded by Tsinghua University on 2/19/2019 7:51:15 AM.

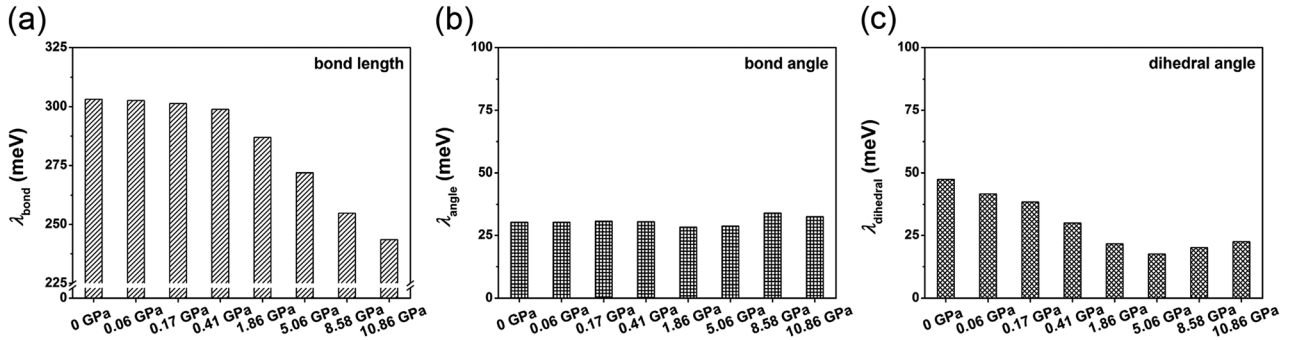

Fig. 9 Projection of the total relaxation energy λ_g onto the internal coordinates of HPS in aggregates at different pressures, including λ_{bond} (a), λ_{angle} (b) and $\lambda_{dihedral}$ (c).

pathways (through-space aromatic-dimer states, π twist and conical intersection)[55–58] to dissipate the excited-state energy are also possible because the actual PES of the excited state is rather complex. Since the solid-state PIEE materials are already emissive at ambient pressure, we simply emphasize in this work that the enhanced emission upon compression arises from restricted intramolecular rotations, which we believe is essential for such series of molecules.

4. Conclusions

In summary, we investigated the pressurization effect on the optical emission of the HPS crystal from first principles combining DFT-D calculations, QM/MM simulations and thermal vibration correlation function formalism. We found that the absorption bands undergo remarkable red-shifts but the emission shifts are minor with increasing pressure up to 10.86 GPa. The radiative rate constants are immune to pressure and vary slightly owing to the almost unaffected electronic transition properties. However, the non-radiative rate constants gradually decrease upon compression at 0–5.06 GPa and then level off, below which it was found that the low-frequency molecular rotations are more susceptible to the molecular packing. In accordance with the excited-state decay rate constants, the fluorescence quantum efficiency exhibits a rapid increase from ~80% (0 GPa) to ~97% (5.06 GPa) and then saturates from there on. The calculated results well reproduce the PIEE experiment for HPS and clarify the relationship between the electronic structure of HPS in aggregates and the luminescent properties at high pressure. The predicted resonance Raman spectra of the HPS crystal at different pressures demonstrate its potential for the characterization of the pressurization effect on the vibrational relaxation and the validation of the above hypothesis in explaining the PIEE mechanism. At the same time, our theoretical protocol is proposed to investigate the excited-state dynamics of other mechano-responsive materials. HPS is also a representative member of the AIE family, which is poorly luminescent in solution but highly emissive in aggregates.[59,60] PIEE is another outcome of such effect since pressurization shortens intermolecular distances and suppresses intramolecular motions. The theoretical study of PIEE in the HPS crystal not only gives support to the existing experimental findings but also paves the way for the rational design of advanced PIEE materials.

Finally, it should be noted that the present methodology we used to treat the spectroscopy and excited-state dynamics here is based on the assumptions of a displaced and distorted harmonic oscillator model. It has been shown previously that both the vibrational quanta and the electronic adiabatic transition energies decrease steadily with molecular size,[49] implying a diminished anharmonic effect for large molecules. The methods have indeed demonstrated superiority and robustness in describing the optical properties of organic aggregates.[18–20,34,61] Nevertheless, there is still a long way to go toward quantitative prediction of solid-state light-emitting quantum efficiency from first-principles by considering the charge transfer delocalization, anharmonicity and non-perturbation, *etc.*

Conflicts of interest

There are no conflicts of interest to declare.

Acknowledgements

This work is supported by the National Natural Science Foundation of China (Grant No. 21788102, 21703122 and 21576159) and the Natural Science Foundation of Shandong Province (Grant No. ZR2017BB034). The support from the Ministry of Science and Technology (Grant No. 2017YFA0204501 and 2015CB655002) and the Scientific Research Foundation of Shandong University of Technology is greatly acknowledged. Great thanks to Jianzhong Fan and Kai Zhang for their great help with the approach to reveal the noncovalent interactions.

References

1 Y. Sagara and T. Kato, *Nat. Chem.*, 2009, **1**, 605–610.
2 Z. G. Chi, X. Q. Zhang, B. J. Xu, X. Zhou, C. P. Ma, Y. Zhang, S. W. Liu and J. R. Xu, *Chem. Soc. Rev.*, 2012, **41**, 3878–3896.
3 W. Z. Yuan, Y. Q. Tan, Y. Y. Gong, P. Lu, J. W. Y. Lam, X. Y. Shen, C. F. Feng, H. H. Y. Sung, Y. W. Lu, I. D. Williams, J. Z. Sun, Y. M. Zhang and B. Z. Tang, *Adv. Mater.*, 2013, **25**, 2837–2843.

 This journal is © The Royal Society of Chemistry 2019

Published on 03 January 2019. Downloaded by Tsinghua University on 2/19/2019 7:51:15 AM.

4 H. B. Sun, S. J. Liu, W. P. Lin, K. Y. Zhang, W. Lv, X. Huang, F. W. Huo, H. R. Yang, G. Jenkins, Q. Zhao and W. Huang, *Nat. Commun.*, 2014, **5**, 3601.
5 Q. K. Qi, J. Y. Qian, X. Tan, J. B. Zhang, L. J. Wang, B. Xu, B. Zou and W. J. Tian, *Adv. Funct. Mater.*, 2015, **25**, 4005–4010.
6 S. Mukherjee and P. Thilagar, *J. Mater. Chem. C*, 2016, **4**, 2647–2662.
7 W. L. Mao, H. K. Mao, P. J. Eng, T. P. Trainor, M. Newville, C. C. Kao, D. L. Heinz, J. F. Shu, Y. Meng and R. J. Hemley, *Science*, 2003, **302**, 425–427.
8 Y. Q. Dong, J. W. Y. Lam and B. Z. Tang, *J. Phys. Chem. Lett.*, 2015, **6**, 3429–3436.
9 S. Bergantin, M. Moret, G. Buth and F. P. A. Fabbiani, *J. Phys. Chem. C*, 2014, **118**, 13476–13483.
10 J. Wu, J. Tang, H. L. Wang, Q. K. Qi, X. F. Fang, Y. F. Liu, S. P. Xu, S. X.-A. Zhang, H. Y. Zhang and W. Q. Xu, *J. Phys. Chem. A*, 2015, **119**, 9218–9224.
11 X. Fan, J. L. Sun, F. Z. Wang, Z. Z. Chu, P. Wang, Y. Q. Dong, R. R. Hu, B. Z. Tang and D. C. Zou, *Chem. Commun.*, 2008, 2989–2991.
12 Q. Wang, S. Y. Li, L. M. He, Y. Qian, X. P. Li, W. H. Sun, M. Liu, J. Li, Y. Li and G. Q. Yang, *ChemPhysChem*, 2008, **9**, 1146–1152.
13 H. S. Yuan, K. Wang, K. Yang, B. B. Liu and B. Zou, *J. Phys. Chem. Lett.*, 2014, **5**, 2968–2973.
14 M. Ouyang, L. L. Zhan, X. J. Lv, F. Cao, W. J. Li, Y. J. Zhang, K. Y. Wang and C. Zhang, *RSC Adv.*, 2016, **6**, 1188–1193.
15 Y. R. Gu, K. Wang, Y. X. Dai, G. J. Xiao, Y. G. Ma, Y. C. Qiao and B. Zou, *J. Phys. Chem. Lett.*, 2017, **8**, 4191–4196.
16 D. C. Sorescu and B. M. Rice, *J. Phys. Chem. C*, 2010, **114**, 6734–6748.
17 B. Schatschneider, S. Monaco, A. Tkatchenko and J.-J. Liang, *J. Phys. Chem. A*, 2013, **117**, 8323–8331.
18 Q. Y. Wu, C. M. Deng, Q. Peng, Y. L. Niu and Z. G. Shuai, *J. Comput. Chem.*, 2012, **33**, 1862–1869.
19 Z. G. Shuai and Q. Peng, *Phys. Rep.*, 2014, **537**, 123–156.
20 T. Zhang, Q. Peng, C. Y. Quan, H. Nie, Y. L. Niu, Y. J. Xie, Z. J. Zhao, B. Z. Tang and Z. G. Shuai, *Chem. Sci.*, 2016, **7**, 5573–5580.
21 G. Kresse and J. Furthmüller, *Phys. Rev. B: Condens. Matter Mater. Phys.*, 1996, **54**, 11169–11186.
22 G. Kresse and D. Joubert, *Phys. Rev. B: Condens. Matter Mater. Phys.*, 1999, **59**, 1758–1775.
23 P. E. Blöchl, *Phys. Rev. B: Condens. Matter Mater. Phys.*, 1994, **50**, 17953–17979.
24 S. Grimme, *J. Comput. Chem.*, 2006, **27**, 1787–1799.
25 P. Sherwood, A. H. de Vries, M. F. Guest, G. Schreckenbach, C. R. A. Catlow, S. A. French, A. A. Sokol, S. T. Bromley, W. Thiel, A. J. Turner, S. Billeter, F. Terstegen, S. Thiel, J. Kendrick, S. C. Rogers, J. Casci, M. Watson, F. King, E. Karlsen, M. Sjøvoll, A. Fahmi, A. Schäfer and C. Lennartz, *J. Mol. Struct. THEOCHEM*, 2003, **632**, 1–28.
26 R. Ahlrichs, M. Bär, M. Häser, H. Horn and C. Kölmel, *Chem. Phys. Lett.*, 1989, **162**, 165–169.
27 W. Smith and T. R. Forester, *J. Mol. Graphics*, 1996, **14**, 136–141.
28 D. Bakowies and W. Thiel, *J. Phys. Chem.*, 1996, **100**, 10580–10594.
29 C. Lee, W. T. Yang and R. G. Parr, *Phys. Rev. B: Condens. Matter Mater. Phys.*, 1988, **37**, 785–789.
30 A. D. Becke, *J. Chem. Phys.*, 1993, **98**, 5648–5652.
31 J. M. Wang, R. M. Wolf, J. W. Caldwell, P. A. Kollman and D. A. Case, *J. Comput. Chem.*, 2004, **25**, 1157–1174.
32 T. Zhang, Y. Q. Jiang, Y. L. Niu, D. Wang, Q. Peng and Z. G. Shuai, *J. Phys. Chem. A*, 2014, **118**, 9094–9104.
33 Y. J. Xie, T. Zhang, Z. Li, Q. Peng, Y. P. Yi and Z. G. Shuai, *Chem. – Asian J.*, 2015, **10**, 2154–2161.
34 X. Y. Zheng, Q. Peng, L. Z. Zhu, Y. J. Xie, X. H. Huang and Z. G. Shuai, *Nanoscale*, 2016, **8**, 15173–15180.
35 J. W. Ochterski, *Gaussian Inc.*, 1999, 1–10.
36 Q. Y. Wu, T. Zhang, Q. Peng, D. Wang and Z. G. Shuai, *Phys. Chem. Chem. Phys.*, 2014, **16**, 5545–5552.
37 W. Q. Li, Q. Peng, H. L. Ma, J. Wen, J. Ma, L. A. Peteanu and Z. G. Shuai, *Chem. Mater.*, 2017, **29**, 2513–2520.
38 C.-P. Hsu, Z.-Q. You and H.-C. Chen, *J. Phys. Chem. C*, 2008, **112**, 1204–1212.
39 Y. L. Niu, W. Q. Li, Q. Peng, H. Geng, Y. P. Yi, L. J. Wang, G. J. Nan, D. Wang and Z. G. Shuai, *Mol. Phys.*, 2018, **116**, 1078–1090.
40 M. Valiev, E. J. Bylaska, N. Govind, K. Kowalski, T. P. Straatsma, H. J. J. Van Dam, D. Wang, J. Nieplocha, E. Apra, T. L. Windus and W. A. de Jong, *Comput. Phys. Commun.*, 2010, **181**, 1477–1489.
41 T. Yanai, D. P. Tew and N. C. Handy, *Chem. Phys. Lett.*, 2004, **393**, 51–57.
42 Y. L. Niu, Q. Peng, C. M. Deng, X. Gao and Z. G. Shuai, *J. Phys. Chem. A*, 2010, **114**, 7817–7831.
43 Q. Peng, Y. P. Yi, Z. G. Shuai and J. S. Shao, *J. Am. Chem. Soc.*, 2007, **129**, 9333–9339.
44 S. H. Lin, *J. Chem. Phys.*, 1966, **44**, 3759–3767.
45 Y. J. Yan and S. Mukamel, *J. Chem. Phys.*, 1986, **85**, 5908–5923.
46 H. L. Ma, J. Liu and W. Z. Liang, *J. Chem. Theory Comput.*, 2012, **8**, 4474–4482.
47 E. R. Johnson, S. Keinan, P. Mori-Sánchez, J. Contreras-García, A. J. Cohen and W. Yang, *J. Am. Chem. Soc.*, 2010, **132**, 6498–6506.
48 W. Q. Li, Q. Peng, Y. J. Xie, T. Zhang and Z. G. Shuai, *Acta Chim. Sin.*, 2016, **74**, 902–909.
49 Y. Q. Jiang, Q. Peng, X. Gao, Z. G. Shuai, Y. L. Niu and S. H. Lin, *J. Mater. Chem.*, 2012, **22**, 4491–4501.
50 T. Zhang, H. L. Ma, Y. L. Niu, W. Q. Li, D. Wang, Q. Peng, Z. G. Shuai and W. Z. Liang, *J. Phys. Chem. C*, 2015, **119**, 5040–5047.
51 E. J. Heller, R. Sundberg and D. Tannor, *J. Phys. Chem.*, 1982, **86**, 1822–1833.
52 F. Santoro, C. Cappelli and V. Barone, *J. Chem. Theory Comput.*, 2011, **7**, 1824–1839.
53 C. Fang, Y. J. Xie, M. R. Johnston, Y. Ruan, B. Z. Tang, Q. Peng and Y. Tang, *J. Phys. Chem. A*, 2015, **119**, 8049–8054.
54 J. R. Reimers, *J. Chem. Phys.*, 2001, **115**, 9103–9109.
55 X.-L. Peng, S. Ruiz-Barragan, Z.-S. Li, Q.-S. Li and L. Blancafort, *J. Mater. Chem. C*, 2016, **4**, 2802–2810.
56 S. Sasaki, S. Suzuki, W. M. C. Sameera, K. Igawa, K. Morokuma and G.-i. Konishi, *J. Am. Chem. Soc.*, 2016, **138**, 8194–8206.

57 J. Sturala, M. K. Etherington, A. N. Bismillah, H. F. Higginbotham, W. Trewby, J. A. Aguilar, E. H. C. Bromley, A.-J. Avestro, A. P. Monkman and P. R. McGonigal, *J. Am. Chem. Soc.*, 2017, **139**, 17882–17889.
58 K. Kokado, T. Machida, T. Iwasa, T. Taketsugu and K. Sada, *J. Phys. Chem. C*, 2018, **122**, 245–251.
59 B. Z. Tang, X. W. Zhan, G. Yu, P. P. S. Lee, Y. Q. Liu and D. B. Zhu, *J. Mater. Chem.*, 2001, **11**, 2974–2978.
60 J. W. Chen, C. C. W. Law, J. W. Y. Lam, Y. P. Dong, S. M. F. Lo, I. D. Williams, D. B. Zhu and B. Z. Tang, *Chem. Mater.*, 2003, **15**, 1535–1546.
61 Z. G. Shuai and Q. Peng, *Natl. Sci. Rev.*, 2017, **4**, 224–239.

Published on 03 January 2019. Downloaded by Tsinghua University on 2/19/2019 7:51:15 AM.

This journal is © The Royal Society of Chemistry 2019